

# An Investigation of Influence of Windshield Configuration and Train Length on High-Speed Train Aerodynamic Performance

A. Adamu<sup>1</sup>, J. Zhang<sup>1,2,3†</sup>, F. Gidado<sup>1</sup> and F. Wang<sup>1,2,3</sup>

<sup>1</sup>Key Laboratory of Traffic Safety on Track of Ministry of Education, School of Traffic & Transportation Engineering, Central South University, Changsha, 410075, China

<sup>2</sup>Joint International Research Laboratory of Key Technology for Rail Traffic Safety, Central South University, Changsha 410075, China

<sup>3</sup>National & Local Joint Engineering Research Center of Safety Technology for Rail Vehicle, Changsha 410075, China

†Corresponding Author Email: [j.zhang@csu.edu.cn](mailto:j.zhang@csu.edu.cn)

(Received July 12, 2022; accepted October 3, 2022)

## ABSTRACT

The aerodynamic performance of four train models with different windshield configurations (i.e., internal and/or external) in three train marshalling modes (i.e., 3, 6 and 8-car groups) was numerically investigated in this study. The train's airflow characteristics at  $Re=2.25\times 10^6$  were determined using the shear stress transport (SST)  $k-\omega$  turbulence model. The results were validated by comparing the pressure distributions and drag forces on the streamlined heads with experimental data. The difference in windshield configuration and train length has a substantial influence on the train's flow field and surface pressure distribution. For the trains with internal windshields, due to non-uniform geometry, the flow is separated and vortices are formed at the windshield area. The boundary layer profile increases with the increased train length, and its thickness varies with windshield configurations. Asymmetric vortices are formed in the wake at a distance close to the tail car's nose, except for trains with external windshields. The reduction of the flow velocity as the train length increases causes a reduction of the low pressure near the tail car's streamline transition, thus causing a decrease in the tail car's drag and lift forces. Consequently, for trains with external windshields, the head car's drag increases, whereas the total train drag reduces significantly as the train length increases. Therefore, employing external windshields in all the inter-carriage gap sections, irrespective of the train length, demonstrates a good ability to reduce future train's aerodynamic drag.

**Keywords:** High-speed train; Windshield configuration; Drag force; Flow field; Pressure distribution.

## 1. INTRODUCTION

The high-speed train (HST) has become one of the most essential parts of today's ground transportation system due to its fast speed and high transport efficiency. The train aerodynamic characteristics, i.e., aerodynamic drag/lift forces, slipstream, and aerodynamic noise, are important parameters for the design of a new HST. The continuous rise in HST operational speed has caused concerns about the train's aerodynamic performance, especially the aerodynamic drag related to energy consumption. The aerodynamic drag is the resistance force felt by the train as it moves in open air (Zhang *et al.* 2018; Zhou *et al.* 2021; Sun *et al.* 2020; Tan *et al.* 2022), and increases as the train speed increases (Baker

2014; Tian 2007). Thus, for researchers, optimizing the train shape to achieve drag reduction has become a crucial issue.

To decrease energy utilization and increase the train travelling speed, much research has been conducted to improve the geometry of the HST. Recently, more emphasis has been placed on the geometric optimization of the discontinuous sections of the train, including the bogie cavities, cowcatchers, inter-carriage gaps and so on (Wang *et al.* 2020; Niu *et al.* 2018b; Niu *et al.* 2019; Zhang *et al.* 2022a; 2022b; Tang *et al.* 2022). This paper will concentrate on the improvement of the inter-carriage structure for drag reduction.

Effective optimization of the inter-carriage structure through the application of windshields (internal and/or external) has the ability to improve HST aerodynamics. To determine the effect of inter-carriage structures on the HST aerodynamics, Kukreja and Jumar (2016) employed a two-dimensional model to investigate the turbulent flow in an Indian train's inter-carriage gap. They found that vortices are formed in the inter-carriage gap region, and the train drag is decreased by 4% to 5% when the gaps are effectively enclosed. Zhang *et al.* (2022) examined the impact of simplification of train bogie regions on the HST aerodynamics. They reported that the train's drag coefficient reduced by 38.2% and 30.3%, respectively, for HST with no surface roughness and those with smoothed inter-car gap/bogie cavities. Niu *et al.* (2019) investigated the impact of the external windshield configuration on the train aerodynamic characteristics using six different configurations, employing experiments and numerical simulations. They demonstrated that a completely covered external windshield increases the head car's drag, whereas the total train drag is reduced (Du *et al.* 2020).

The similarity criterion is the fundamental premise for reduced-scale tests, and geometric similarities are required to achieve complete similarity between the actual and model train flow fields (CEN European Standard. 2010; Munson *et al.* 2015). Real trains in operation are usually 8 cars or 16 cars, but in reduced-scale experiments, short-length trains (i.e., 3-car group trains) are mostly employed. The variation of train length may lead to a difference between the results of the reduced scale tests and full-scale experiments, as it is difficult to ensure a similar Reynolds number due to wind tunnel/test rig size constraints. Sicot *et al.* (2018) carried out a wind tunnel experiment to investigate the impact of the replica scale of structural components on trains in wind tunnel experiments. The results revealed that differences in the replica scale have a substantial effect on the aerodynamic quantities recorded in the experiment. In numerical simulations, the train geometry can be modelled to have similar features to those of the actual train; thus, the flow features of HSTs having different train lengths can be studied. Muld *et al.* (2014) studied the flow characteristics of HSTs with three different lengths. They demonstrated that varying boundary layer thicknesses cause variable shedding frequencies and vortices in the wake (Yang *et al.*, 2022). Tan *et al.* (2020) showed that when a train's length increases, the mean drag and lift coefficient of the tail car reduces significantly. Consequently, the averaged drag coefficients for the tail cars of trains with 4-car and 8-car groups are reduced by 28 % and 44% as compared to a 2-car group train. Chen *et al.* (2022) investigated the effect of the train length on its aerodynamics, mainly concentrating on the flow mechanism. The results revealed that with increased train length, so does the boundary layer thickness and instantaneous velocity inside the boundary layer. This leads to a highly turbulent kinetic energy distribution

and a flow velocity reduction near the tail car's streamlined area. The decrease in flow velocity causes a decrease in negative pressure, which decreases the tail car's drag and lift forces.

The purpose of this investigation can be highlighted as follows:

- As demonstrated from the articles above, the application of an external windshield in all the inter-carriage sections can increase the head car's aerodynamic drag, while it decreases for the tail car (Niu *et al.* 2019). In this study, the flow fields surrounding the inter-carriage section are investigated to understand the flow characteristics and to optimise not only the head and the tail car's aerodynamic performance, but also that of the HST using internal and/or external windshields. Consequently, four windshield configurations are studied.
- In addition, as the HST aerodynamic performance varies with the train length, the influence of variation of the windshield configuration is studied using three different train lengths. This will give an understanding of the aerodynamic characteristics and the amount of improvement that can be achieved as the train length increases. Thus, four windshield configurations in 3, 6 and 8-car group trains are investigated.

The SST  $k-\omega$  turbulence model, which has been proven to accurately predict the train aerodynamic forces (Xia *et al.* 2020; Zhang *et al.* 2022a; 2022b; Wang *et al.* 2022), is employed to investigate the flow fields surrounding the train models.

This work is structured as follows: Section 2 describes the geometry, computational domain and boundary conditions, computational mesh, the methodology for CFD analysis, and formulations for data processing. In Section 3, the grid independence study and numerical method validation are described. Section 4 evaluates the numerical data, while conclusions are given in Section 5.

## 2. COMPUTATIONAL SET-UPS

### 2.1. Geometry

A simple 1:7 scale ICE3 (Inter-city express 3) HST model was used in this work. The train has the following full-scale measurements: height  $H=3.890$  m, length  $L=76.445$  m, and width  $W=2.950$  m. The length of the head as well as the tail car is 25.835 m, while it is 24.774 m for the middle car. The train length is  $(25.835 \text{ m} \times 2) + (N - 2) \times 24.775$  m; where N is either 3, 6, or 8.

To simplify the HST model, the pantograph and other ancillary components were deleted, except the inter-car structures and bogies. Furthermore, in order to maintain consistency with the ground case setups in the CEN Standard, track-bed was not employed.

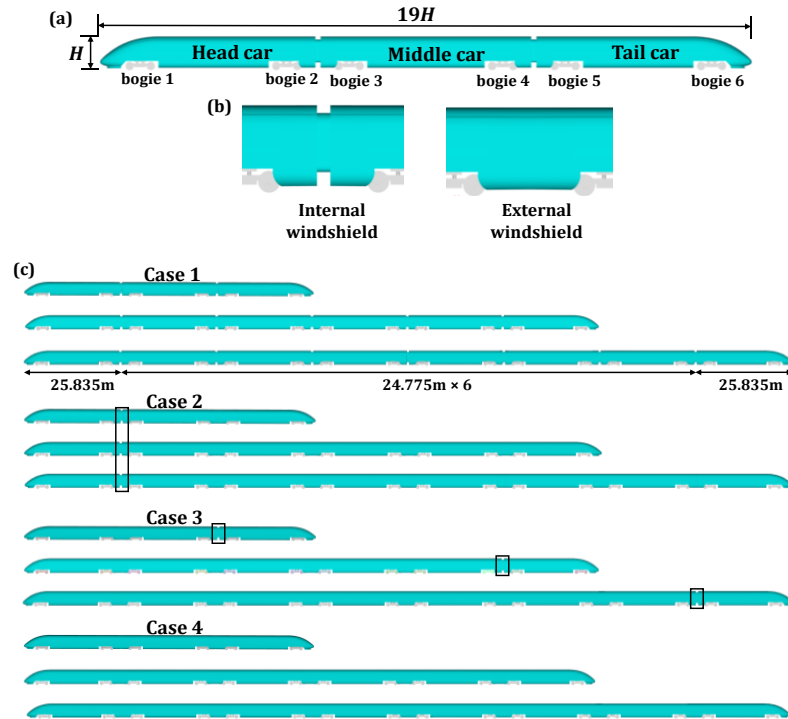


**Fig. 1.** Simplified ICE 3 train model (a). Internal and external windshields (b). Cases 1-4 with different windshield configurations in 3, 6 and 8-car groups (c).

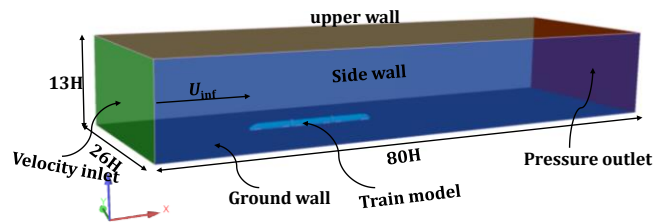


**Fig. 2.** Computational domain.

To examine the effect of windshield configurations on train aerodynamics, the internal and external windshields presented in Fig. 1(b) were used. Four train models denoted as Case 1, Case 2, Case 3 and Case 4 in three grouping modes (i.e., 3, 6 and 8-car group trains) with different windshield configurations are employed as highlighted in Fig. 1(c). Case 1 is a train with an internal windshield in all the inter-carriage sections. Case 2 is a train with an internal windshield in the first inter-carriage section while the other inter-carriage sections are covered with an external windshield. In Case 3, external windshields are used in all the inter-carriage sections except the last section, while all of the inter-carriage gap sections are covered with external windshields in Case 4.

## 2.2. Computational Domain and Boundary Conditions

To examine the HST aerodynamics, the train was positioned in the centre of a computational domain as

highlighted in Fig. 2. Based on the CEN standard for HSTs, the inlet of the computational domain has to be at least  $8H$  away from the head nose and tail nose to the outlet should be at least  $16H$  (CEN European Standard 2010). However, the length of the domains used in this work is slightly longer to prevent boundary interference and to permit wake formation.

The domain has a height of  $13H$  and a width of  $26H$ . The inlet is placed at  $18H$  from the head nose, whereas the length from the tail nose to the outlet is  $42H$  for the 3, 6 and 8-car group trains.

According to the uniform inlet velocity  $U_{inf} = 60$  m/s and the train height  $H = 0.5557$  m, the Reynolds number  $Re = \rho U_{inf} H / \mu \approx 2.25 \times 10^6$ . The symmetry boundary condition was used for the back, front, and upper wall. A gauge pressure of 0 Pa was maintained at the outlet. To ensure a relative motion between the lower wall and the train, a moving ground with the inlet velocity is used.

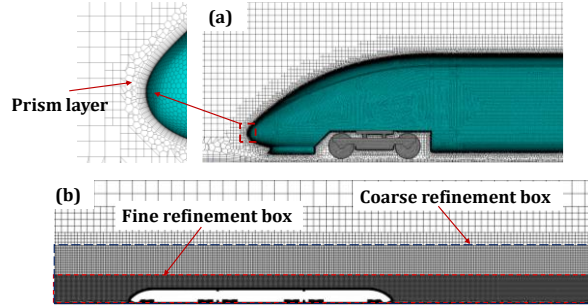


Fig. 3. Mesh distribution on the head car with prism layers (a) and the symmetry plane (b).

### 2.3. Mesh Generation for CFD Simulation

The ANSYS Fluent meshing software, which creates highly automated grids, was used to create the poly-hexahedral dominating grids used in this work.

The accuracy, speed, and convergence of the solution are influenced by the mesh quality. Consequently, two refinement boxes were placed around the train to precisely capture the flow features and increase the reliability of the numerical computations. Fine meshes are formed on the surface of the train, while coarse meshes are in the outer region, as highlighted in Fig. 3.

In order to accurately simulate the near-wall flow field, 15 prism layers with an aspect ratio of 35 were placed on the train surface in the spanwise ( $\Delta l$  +) and streamwise ( $\Delta s$  +) directions, in comparing with the first cell height. Due to their small clearance and complex geometry, the bogies and the ground has 10 layers with an aspect ratio of 25. Therefore, 0.11 mm is the height of the first; thus  $y+$  is less than 10 in most part of the train. The same  $y+$  value has been employed in other studies for the SST  $k-\omega$  turbulence model (Niu *et al.* 2018a; Xia *et al.* 2020). Fig. 3 present the distributions of mesh on the symmetry plane, the head car, and the prism layers around the head nose.

### 2.4. Method for CFD simulation

The governing equations in CFD analysis are discretized using the ANSYS Fluent finite volume approach.

The SST  $k-\omega$  turbulence model (where the turbulence kinetic energy is  $k$ , and the specific dissipation rate is  $\omega$ ) was employed. It was created by Menter (1994) by combining a modified  $k-\varepsilon$  model with the normal  $k-\omega$  model. This is an alternative to the standard  $k-\omega$  model. To allow appropriate computation near and far away from the wall, a merging function and a cross-diffusion component in the  $\omega$  equation are included in the SST  $k-\omega$  model. In near-wall regions, the merging function triggers the  $k-\omega$  model, while at places far from the wall, it triggers the  $k-\varepsilon$  model. This makes it more accurate for a large range of flows than the standard  $k-\omega$  model. The SST  $k-\omega$  model is a steady state method; however, because of its ability to predict different turbulent flows,

the model has been widely adopted (Li *et al.* 2018; Xia *et al.* 2020).

The pressure and velocity fields were coupled using the Semi-Implicit Method for Pressure-Linked Equation Consistent (SIMPLE-C) method. To solve the  $k$  and  $\omega$  equations, the second-order upwind was selected. The residual value of  $10^{-6}$  was set for the equation of continuity to guarantee the flow convergence. The convergence was also monitored for the train aerodynamic force coefficients.

### 2.5. Data Analysis

The non-dimensional variables related to the relevant aerodynamic parameters are specified as follows to enable the evaluation and analysis of the four cases' pressure distributions and aerodynamic forces.

$$C_x = \frac{F_x}{0.5\rho U_{inf}^2 S} \quad (1)$$

$$C_z = \frac{F_z}{0.5\rho U_{inf}^2 S} \quad (2)$$

where  $C_x$  and  $C_z$  are the coefficients of drag and lift forces, while  $F_x$  and  $F_z$  are the drag and lift forces.  $S$  is the train's front area ( $S = 0.2041 \text{ m}^2$ ).

The pressure coefficient  $C_p$  is expressed as

$$C_p = \frac{p - p_{ref}}{0.5\rho U_{inf}^2} \quad (3)$$

where  $p$  denotes the local static pressure;  $p_{ref}$  is the reference pressure (taken as 0 Pa); the density of air  $\rho$  at  $15^\circ\text{C}$  is  $1.225 \text{ kg/m}^3$ .

## 3. NUMERICAL VALIDATION

### 3.1. Mesh-Independence Study

To ensure mesh independence on the aerodynamic quantities, three mesh densities, i.e., fine, medium and coarse meshes with approximately  $39.5 \times 10^6$ ,  $26.5 \times 10^6$  and  $19.5 \times 10^6$  cells respectively, were employed to conduct a grid-independence study. The train with internal windshields and a 3-car group mode in Case 1 was employed. Tables 1 and 2 compare the coefficients of drag and lift forces for various mesh densities.

From Table 1, it is seen that irrespective of the car considered, a small discrepancy is recorded. A similar observation is recorded for the lift force coefficients in Table 2. Therefore, the global quantity, i.e., the aerodynamic forces, is independent of the meshes.

The effects of mesh on the distributions of  $C_p$  on the upper symmetry centreline and the side-line at  $z = 0.3H$  (where the characteristic height,  $H=0.5557$  m) for the three meshes are presented in Fig. 4(a) and (b). The  $C_p$  distributions along the upper symmetry centreline and the side-line in the three mesh densities agree well.

Considering the above analysis (i.e., coefficients of

drag and lift as well as surface pressure) for the three mesh densities, and also to save computing resources, it is determined that the medium mesh can be used in this study.

The HST model with a height of 0.5557 m gives  $Re=2.25 \times 10^6$ , at 60 m/s inlet velocity. By employing the same HST model and calculation scale (i.e., 1:7), Zhang *et al.* (2022a) demonstrated that by varying the inlet velocity (i.e., 80 m/s, 60 m/s and 40 m/s), the Reynolds number is varied, while a small discrepancy is recorded for the values of aerodynamic drag force coefficients.

**Table 1. Aerodynamic drag coefficients on three meshes.**

Grids	Cells $\times 10^6$	Head	Middle	Tail	Total
Fine	39.5	0.1255	0.0945	0.1758	0.3958
Medium	26.5	0.1279	0.0947	0.1751	0.3977
Coarse	19.5	0.1297	0.0943	0.1750	0.3990

**Table 2. Aerodynamic lift coefficients on three meshes.**

Grid	Cells $\times 10^6$	(-) Head	Middle	Tail	Total
Fine	39.5	0.0934	0.0090	0.1053	0.0209
Medium	26.5	0.0888	0.0060	0.1043	0.0215
Coarse	19.5	0.0841	0.0040	0.1052	0.0251

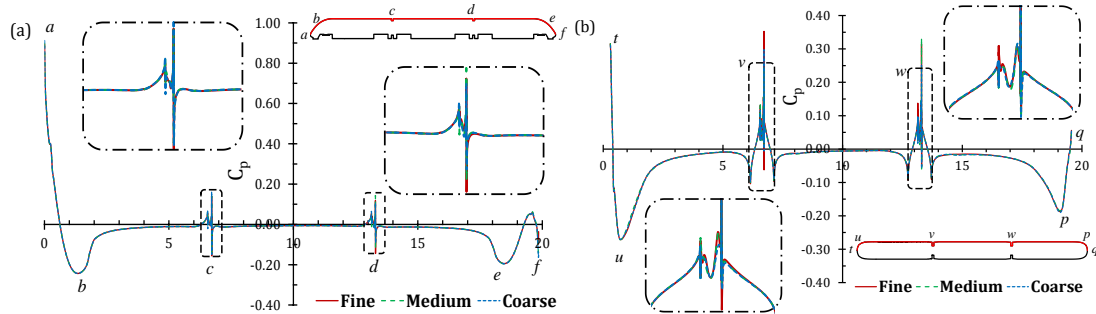


**Fig. 4.  $C_p$  distributions on train models in three mesh densities along (a) the upper surface's symmetry line and (b) the side-line at  $z = 0.3H$ .**

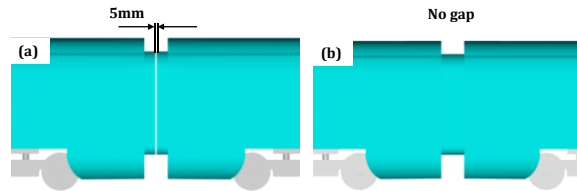


**Fig. 5. Train models with (a) and without (b) gap spacing.**

### 3.2. Validation of the Numerical Method

In wind tunnel experiments, to determine the aerodynamic characteristics of a train (either 3, 6 or 8-car groups), the individual cars, with an appropriate gap between neighbouring vehicles to minimize mechanical contact, are supported by support

ers that are installed separately on balances to measure the aerodynamic forces (Chen *et al.* 2022). Consequently, to verify the simulation method, the impact of the gaps between the neighbouring vehicles is examined. A 5 mm gap spacing is used between the adjacent vehicles of the 3-car group train model of Case 1, as presented in Fig. 5.

**Table 3 Aerodynamic drag coefficients of the train without and with gap spacing compared to experimental data**

Cases	Head	Middle	Tail	Total
Without gap	0.1279	0.0947	0.1751	0.3977
With gap	0.1169	0.0936	0.1838	0.3943
Wind tunnel test (CEN European Standard, 2010)	0.12	-	-	-

From Table 3, the total drag coefficient for the train with gap spacings reduced by 0.9% as compared to that no gaps. The train with gaps shows variation of 2.6%, whereas it is 6.6% for the train with no gap. This indicates that with gap spacings between the vehicles, a similar value as the experimental result can be obtained.

Figure 6 compares the  $C_p$  distribution on the upper symmetry centreline of the head and tail cars to those of the CFD from Dong *et al.* (2020) and experiment (Xia *et al.* 2017). Except for the areas close to the wiper at the tail car, which been deleted in this study, the numerical simulations agreed well with the experimental results.

Since the aerodynamic quantities correlate well with those of the experiments, the CFD methodology is adequate to achieve accurate results and can be adopted for further study.

#### 4. RESULTS AND DISCUSSION

This section examines the results of the impact of the windshield configuration and train length on the train aerodynamics. Firstly, the aerodynamic forces, which include drag and lift forces, are evaluated. After that, the impact of the windshield and length of the trains on the flow features around the train is described. Then, the pressure distribution on the trains is analysed.

##### 4.1. Force Analysis

The configuration of the windshield (both internal and external) and the length of an HST have a substantial impact on the train aerodynamic forces (Li *et al.* 2019; Tan *et al.* 2020), as they directly impact the flow field surrounding the windshield region and the entire train as the length increases. In the present section, the force coefficients (i.e., drag and lift force) of the trains, obtained from numerical simulation in the four cases (with each case having 3, 6 and 8-car group trains) are analysed.

##### 4.1.1. Aerodynamic Drag Forces

To analyse the train aerodynamics, Table 4 compares the drag coefficients in the four cases for 3, 6 and 8-car group trains. In each case, with increased train length, the discrepancy of the drag coefficients of the head car is small and negligible. For the middle car, as the length increases, the aerodynamic drag forces recorded from the second to the last middle car (i.e.,  $M_2-M_6$ ) for the 6 and 8-car grouping mode decrease as compared to the first one (i.e.,  $M_1$ ). For the tail car, when compared to

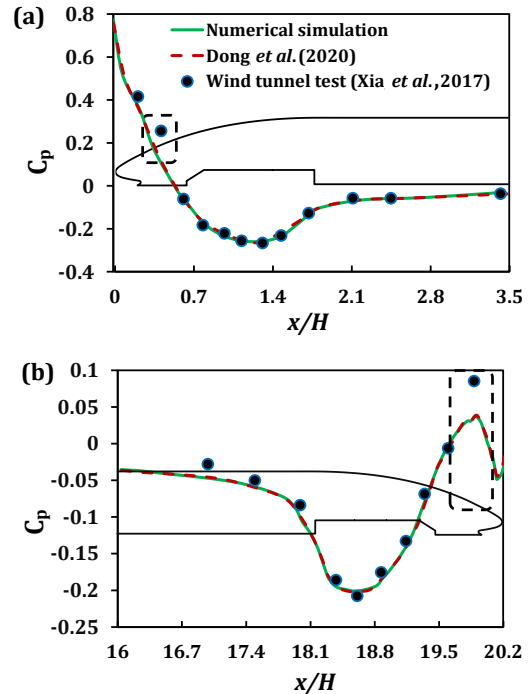


**Fig. 6. Comparison of  $C_p$  along upper centreline of the head (a) and tail cars (b) between experiment (Xia *et al.* 2017), simulation result from Dong *et al.* (2020) and the current study (Zhang *et al.* 2022).**

the 3-car group trains, the  $C_x$  decreases by 11.4% and 15.6% respectively, for the 6 and 8-car grouping in Case 1. However, for Cases 2–4, the tail car’s drag for the 6 and 8-car groupings decreases by 12.5% and 16.0%, 13.8% and 17.7%, and 13.3 and 17.6%, respectively. When the total drag of the trains in the 6 and 8-car groupings are compared to the 3-car grouping for each case, a drag increase of 52.5% and 87.1% is recorded in Case 1, 47.1% and 79.9% in Case 2, 48.1% and 78.6% in Case 3 and 48.2% and 78.8% in Case 4, respectively. This analysis indicates that the train length significantly impacts the drag of the middle and tail cars.

When the first inter-carriage gap is covered with an external windshield, the head car’s drag increases, whereas, when the last inter-carriage gap is covered with an external windshield, the tail car’s drag decreases significantly. For 3-car group trains, in comparison with Case 1, the head car’s drag decreases by 0.7% in Case 2, while it increases by 19.3% and 18.9% in Case 3 and Case 4. However, for the 6 and 8-car

**Table 4. Aerodynamic drag coefficients of 3, 6 and 8-car groupings in Cases 1–4**

Case 1	Component								
	Head car	$M_1$	$M_2$	$M_3$	$M_4$	$M_5$	$M_6$	Tail car	Total
3 cars	0.1279	0.0947	-	-	-	-	-	0.1751	0.3977
6 cars	0.1265	0.0932	0.0812	0.0744	0.0769	-	-	0.1542	0.6064
8 cars	0.1264	0.0933	0.0827	0.0740	0.0730	0.0745	0.0722	0.1478	0.7441
Case 2	Component								
	Head car	$M_1$	$M_2$	$M_3$	$M_4$	$M_5$	$M_6$	Tail	Total
3 cars	0.1270	0.1150	-	-	-	-	-	0.1508	0.3928
6 cars	0.1261	0.1160	0.0731	0.0670	0.0661	-	-	0.1325	0.5811
8 cars	0.1265	0.1188	0.0730	0.0670	0.0654	0.0635	0.0641	0.1284	0.7067
Case 3	Component								
	Head car	$M_1$	$M_2$	$M_3$	$M_4$	$M_5$	$M_6$	Tail car	Total
3 cars	0.1526	0.0661	-	-	-	-	-	0.1764	0.3951
6 cars	0.1523	0.0867	0.0740	0.0674	0.0495	-	-	0.1551	0.5850
8 cars	0.1520	0.0866	0.0745	0.0671	0.0654	0.0648	0.0481	0.1507	0.7092
Case 4	Component								
	Head car	$M_1$	$M_2$	$M_3$	$M_4$	$M_5$	$M_6$	Tail car	Total
3 cars	0.1521	0.0870	-	-	-	-	-	0.1509	0.3903
6 cars	0.1520	0.0866	0.0738	0.0672	0.0651	-	-	0.1336	0.5783
8 cars	0.1519	0.0866	0.0740	0.0672	0.0647	0.0638	0.0643	0.1286	0.7011

group trains, the head cars of Case 3 experienced a drag increase of 20.4% and 20.7% while it is 20.2% in Case 4. For the middle cars, when the drag of the first middle car (i.e.,  $M_1$ ) is compared, a drag increase of 21.4% is recorded in Case 2, while it decreased by 9.1% in Case 3 and 8.1% in Case 4 as compared to Case 1 for 3-car group trains, and similarly for the 6 and 8-car group trains. The tail car experiences a significant drag reduction when an external windshield is used at the last inter-carriage gap section. The tail car’s drag in Case 2 and Case 4 decreases by 13.9% and 13.8% as compared to Case 1 for 3-car group trains. When the train length increases, the drag reduces by 14.1% and 13.1% for the 6 and 8-car group trains in Case 2, while it is 13.4% and 12.9% in Case 4. When the total train drag is evaluated, a drag reduction of 1.5%, 1.3% and 2.0% is achieved in Cases 2–4 as compared to Case 1, for 3-car group trains. When the train length increases, the drag reduces by 4.2%, 3.7% and 4.7% for the 6-car group trains, and 5.0%, 4.7% and 5.2% respectively, for 8-car group trains.

These analyses indicate that the head car’s drag increases significantly with external windshields in all the inter-carriage gaps, whereas the total train drag decreases. When an internal windshield is employed at the first inter-carriage section, the head and tail car drag decreases significantly. When the total train drag is compared, the train with an external windshield has the highest drag reduction. As the train length increases, more drag reduction is achieved.

**4.1.2. Aerodynamic lift forces**

To determine the impact of the windshield configurations and train length on the aerodynamic lift

forces, Table 5 presents the lift coefficients ( $C_z$ ) for 3, 6, and 8-car group trains in Cases 1–4.

The  $C_z$  of the head car in all cases is within small negative values, while those of the tail cars are positive (note that high positive lift forces of the tail car may lead to sway issues), as shown in Table 5. As the windshield configuration varies and the train length increases, different values of aerodynamic lift forces are recorded for the middle cars in all cases. The lift forces recorded for the first middle cars (i.e.,  $M_1$ ) for Case 1, 3 and 4 are positive values, whereas those of Case 2 are negative. This indicates higher stability for the first middle car in Case 2 than in other cases. In Case 1, as the train length increases, the total lift force decreases, with the 8-car grouping having a negative value. A similar decrease in lift force is seen in Case 4; however, the lift forces are positive for all train lengths. As observed in Table 5,  $C_z=0.0200$  for all train lengths in Case 2. This indicates that increase of the train length has little or no impact on the lift force. In Case 3, as the marshalling length increases, the total lift force first increases and then decreases.

The variation of windshield configuration and train length causes significant variation in the train aerodynamic lift forces; however, for all cases, the total lift coefficients are small compared to the drag forces and may have a negligible impact on the train aerodynamics.

**4.2. Flow Distribution around Trains**

As HST moves in open air, a flow field is formed around it due to the air’s viscous effect. To investigate the flow characteristics around trains, [Tian \*et al.\* \(2015\)](#)

**Table 5. Aerodynamic lift coefficient for 3, 6 and 8-car groupings in Cases 1–4**

Case 1	Component								
	Head car	$M_1$	$M_2$	$M_3$	$M_4$	$M_5$	$M_6$	Tail car	Total
3 cars	-0.0888	0.0060	-	-	-	-	-	0.1043	0.0215
6 cars	-0.0906	0.0062	0.0088	-0.0007	-0.0059	-	-	0.0832	0.00097
8 cars	-0.0889	0.0068	0.0075	-0.0008	-0.0008	-0.0085	-0.0071	0.0844	-0.0076
Case 2	Component								
	Head car	$M_1$	$M_2$	$M_3$	$M_4$	$M_5$	$M_6$	Tail car	Total
3 cars	-0.0902	-0.0025	-	-	-	-	-	0.1126	0.0200
6 cars	-0.0890	-0.0025	0.0010	0.0014	-0.0002	-	-	0.1093	0.0200
8 cars	-0.0887	-0.0014	0.0015	0.0007	0.0016	0.0018	0.00006	0.1046	0.0200
Case 3	Component								
	Head car	$M_1$	$M_2$	$M_3$	$M_4$	$M_5$	$M_6$	Tail car	Total
3 cars	-0.0950	0.0146	-	-	-	-	-	0.1039	0.0236
6 cars	-0.0941	0.0054	0.0020	0.0039	0.0146	-	-	0.0924	0.0242
8 cars	-0.0954	0.0056	0.0016	0.0009	0.0020	0.0014	0.0152	0.0884	0.0196
Case 4	Component								
	Head car	$M_1$	$M_2$	$M_3$	$M_4$	$M_5$	$M_6$	Tail car	Total
3 cars	-0.0944	0.0044	-	-	-	-	-	0.1134	0.0234
6 cars	-0.0950	0.0053	0.0013	0.0008	0.0007	-	-	0.1088	0.0220
8 cars	-0.0972	0.0055	0.0017	0.0006	0.0016	0.0015	-0.0011	0.1013	0.0139

placed the inter-carriage section and the under-body structure in high turbulence regions. This is because of the discontinuous geometry of these regions, which promotes the formation of vortices and flow separations. Therefore, to examine the effect of the windshield configuration and train length on the flow field, Fig. 7 presents the velocity contours in the symmetry plane at the first ( $F_w$ ) and last ( $L_w$ ) windshield areas for 3, 6 and 8-car group trains in Cases 1–4 respectively. The internal windshield is divided into 2 regions (i.e.,  $T_1$  and  $T_2$ ), as highlighted in Fig. 7.

The variations of train length and windshield configuration directly impact the flow surrounding the HST, hence affecting the train aerodynamic characteristics. For the trains with internal windshields, due to the non-uniform geometry of the train surface in those regions, the flow is separated and vortices are formed at both  $T_1$  and  $T_2$ . However, no flow separation is observed in the regions with external windshields. The streamwise flow at the upper part of the train is higher for the  $F_w$  area and decreases significantly at the  $L_w$  area with increased train length. Below the windshield, the velocity of the airflow is lower than at the upper part, and a reduction in flow velocity is observed due to the underbody complexity and inter-carriage structures (for areas with internal windshields), which is also observed by [Chen \*et al.\* \(2022\)](#). At the upper part of the internal windshield region of Cases 1–3, vortices are formed at  $T_1$  for all train lengths due to the high flow velocity and non-uniform geometry. Similarly, vortices are observed at  $T_2$ , except for the  $F_w$  and  $L_w$  areas of the 6-car grouping in Case 1, the  $F_w$  area for the 8-car grouping in Case 2 and the  $L_w$  area of Case 3.

At the  $F_w$  area of Cases 1 and 2, since the windshield configurations are the same, similar flow structures are

observed; similarly in Case 3 and Case 4 for 3, 6 and 8-car group trains. Overall, the flow at the  $F_w$  and  $L_w$  areas of Case 4 is higher, followed by Case 2 at the  $L_w$  area.

To analyse the effect of the windshield configuration and train length on the wake flow, Fig. 8 presents the flow velocity contours around the nose of the rear cars. The air coming from the tail car’s top streamline combines with that from the lower part, thus generating separation bubbles beneath the nose and near the cowcatcher in all cases. The variations in the windshield configurations and train length cause significant differences in the flow topology in the cowcatcher areas. In the rear, a variable reattachment area is evident where the flow structure and velocity distribution vary significantly, as seen in Fig. 8. The pair of separation bubbles that are formed at the cowcatcher area of Case 4 for 3, 6 and 8-car group trains shows a clear diffusion. Cases 1 and 2 have greater low-velocity areas than Cases 3 and 4, demonstrating that those separations allow the flow’s kinetic energy to dissipate.

[Muld \*et al.\* \(2014\)](#) demonstrated that, as the train length increases, the varying boundary layer thicknesses cause variable shedding frequencies and vortices in the wake. To further explore the flow at the wake, the vertical planes in Figs. 9–11 show the velocity contour at distances of  $0.05H$ ,  $0.15H$ , and  $0.30H$  from the tail nose, for the 3, 6 and 8-car trains in the four cases.

According to Fig. 9, vortices are seen at  $0.3H$  from the tail nose, whose topology becomes asymmetric with increased train length. A similar observation was made by [Jia \*et al.\* \(2017\)](#). When the vertical plane is at  $0.15H$ , the asymmetric counter-rotating vortices are more visible except for the 3-car group trains in Case 1, 3 and 4, as shown in Fig. 10. The vortex sizes and velocity

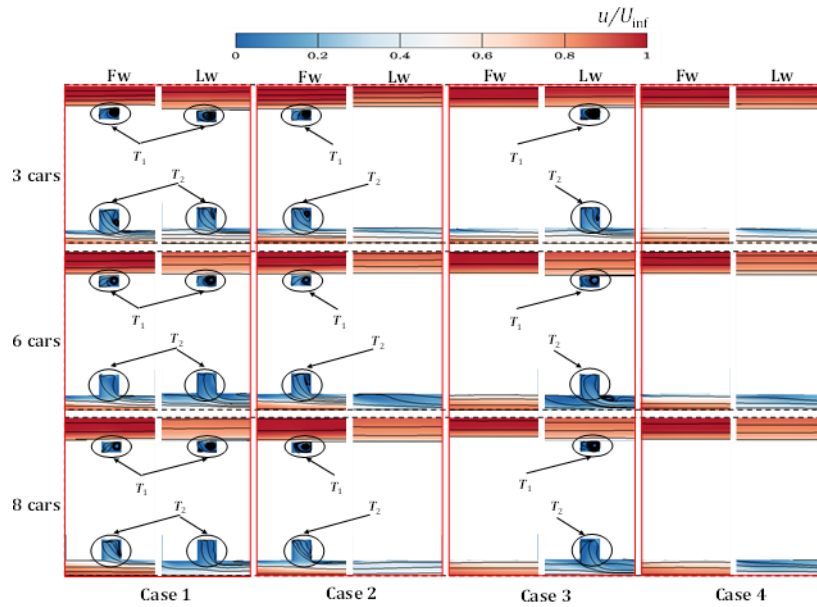


Fig. 7. Velocity contours in the symmetry plane around the first (*Fw*) and last (*Lw*) windshield areas for 3, 6 and 8-car groups in Cases 1–4.

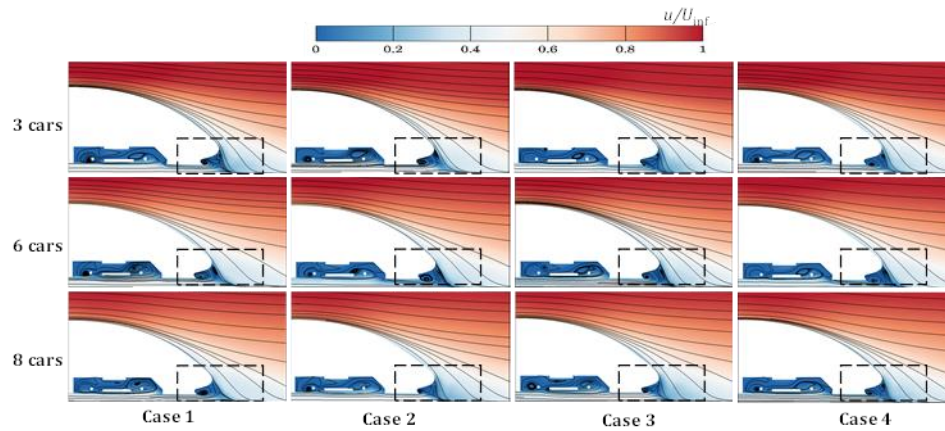


Fig. 8. Velocity contours drawn with streamlines in the tail car's symmetry plane in Cases 1–4.

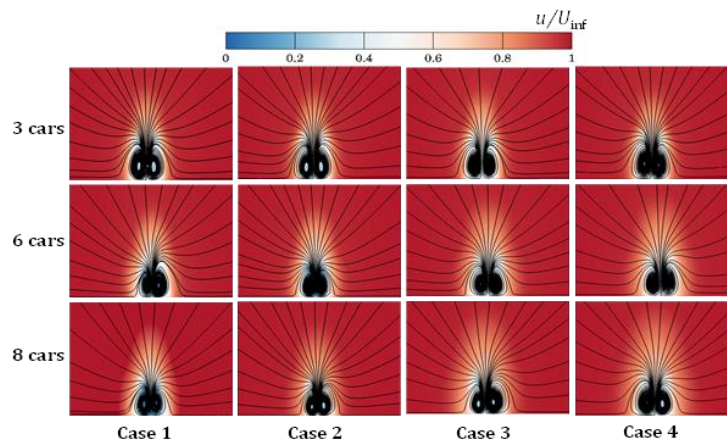
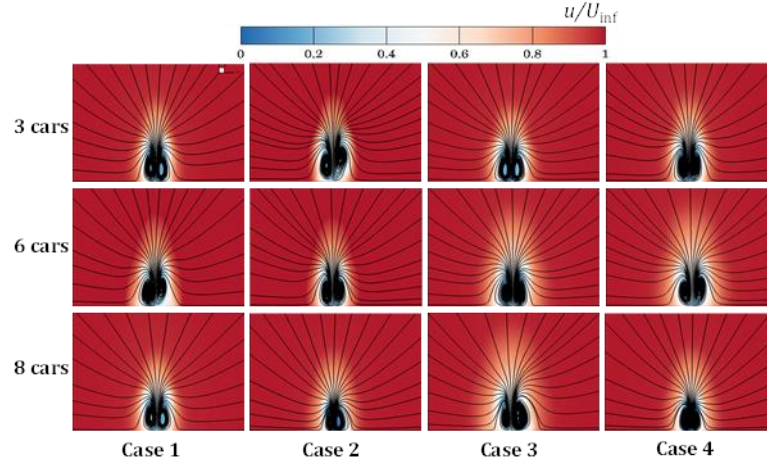
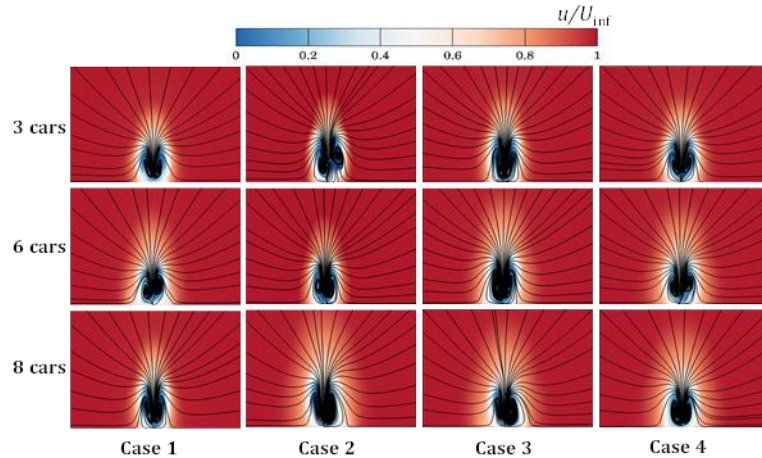


Fig. 9. Streamlines in vertical planes at  $0.3H$  from the tail car nose for 3, 6, and 8-car group trains in four cases respectively.



**Fig. 10.** Streamlines in vertical planes at  $0.15H$  from the tail car nose for 3, 6, and 8-car group trains in four cases respectively.



**Fig. 11.** Streamlines in vertical planes at  $0.05H$  from the tail car nose for 3, 6, and 8-car group trains in four cases respectively.

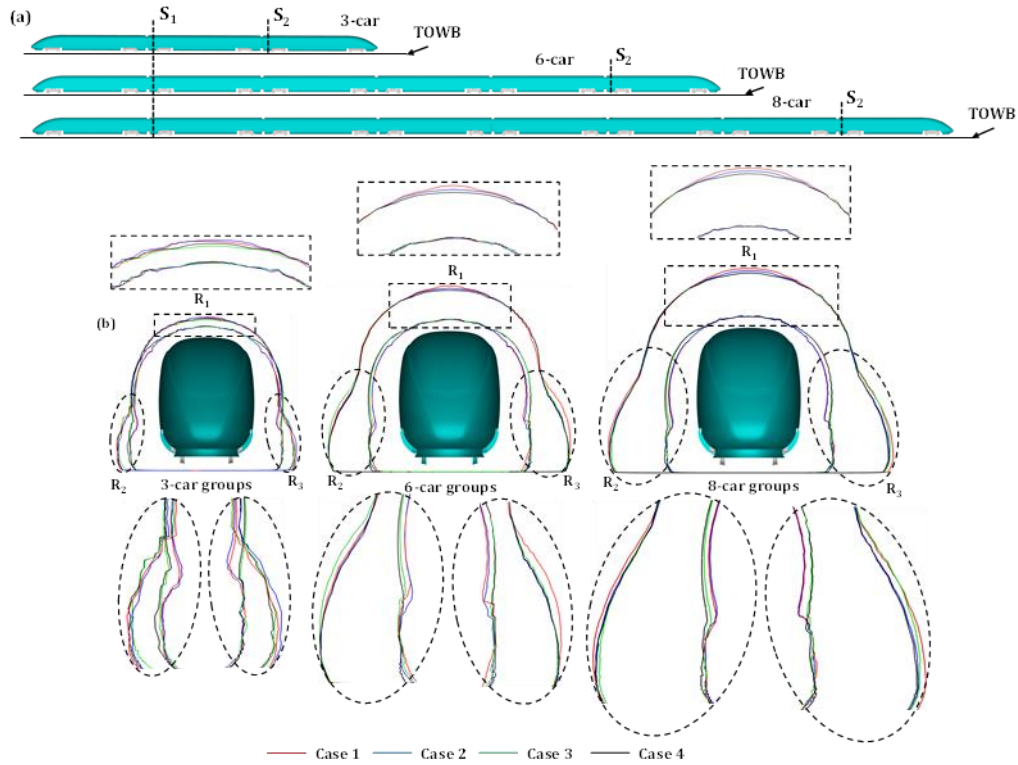
are reduced at  $0.05H$ , and the asymmetric nature of the vortices increases, especially in Case 1 and Case 2, as highlighted in Fig. 11. In all cases, the velocity decreases as the vortices get smaller. Overall, variations of windshield configurations and length of the train show a significant effect on the vortex structure formed at the wake.

Figure 12 highlights the boundary layer distributions on sections  $S_1$  and  $S_2$  (where  $S_1$  is located at  $7H$  in all cases, while  $S_2$  is located at  $13.7H$ ,  $34.4H$  and  $48H$  for the 3, 6 and 8-car groupings from the head nose) in the four cases. The boundary layer at  $S_2$  is thicker than that at  $S_1$ . This is consistent with the typical trend that the boundary layer thickness increases with the train length (Zhang *et al.* 2018).

As demonstrated in Fig. 12, the variation in the windshield configurations causes a discrepancy in the thickness of the upper part boundary layer ( $R_1$ ) and sides ( $R_2$  and  $R_3$ ). However, at the bottom, because of

the moving floor boundary condition employed for simulations, boundary layers effect on the floor is eliminated. At the upper part, the variation in the profiles at  $S_2$  is significantly greater than that of  $S_1$  for all cases. For the 3-car group trains, Case 1 and Case 2 have a thicker profile at  $S_2$  than Case 3 and Case 4. However, at the upper part of the 6 and 8-car group trains, Case 1 has a thicker boundary layer profile, followed by Case 2 at  $S_2$ .

A significant variation in the boundary layer thickness in the four cases is observed at  $R_2$  and  $R_3$  due to the variations in windshield configurations and the complex nature of the flow in the space between the train's bottom and the ground (Niu *et al.* 2018b). At  $S_1$ , for all train lengths, Case 1 and Case 2 have similar boundary layer thicknesses, while those of Case 3 and Case 4 are similar. At  $S_1$ , for 3-car group trains, Case 4 has a thicker boundary layer at  $R_2$  and  $R_3$  while Case 2 has a thicker profile at  $S_2$ . For 6 and 8-car group trains, Case 4 has a thicker boundary layer at  $S_1$ ; however, at



**Fig. 12. Locations of  $S_1$  and  $S_2$  (a) and boundary layer thickness of trains with 3, 6 and 8-cars for Cases 1–4 at  $S_1$  and  $S_2$  (b).**

section  $S_2$ , Case 3 has a thicker profile at the lower part (i.e.,  $R_2$ ). This indicates that with the variation of windshield configurations and train length, the airflow structures near the windshield at below the train height and the top is substantially impacted. Consequently, this affects the thickness of boundary layer, causing a difference in the viscous drag and the total aerodynamic resistance recorded in the various cases, as noted in Table 4.

As the train length increases, the layer becomes thicker, which results in a decrease in the streamwise velocity around the rear car's streamline region. The reduction in the flow velocity results in a reduction in the negative pressure, as shown in Figs. 13 and 15, thus causing a decrease in the drag as well as the lift coefficients of the rear car.

### 4.3. Train Pressure Distributions

The pressure on various parts of an HST affects its aerodynamic performance, as the pressure force on the train takes a dominant part of the aerodynamic forces (Baker 2010).

Figure 13 presents the  $C_p$  distributions at the upper symmetry centreline of 3, 6 and 8-car group trains in Cases 1–4 respectively. In Case 1, a large fluctuation is observed in the windshield areas and the head and tail car's streamlined region. The length of the train has

little or no impact on the train head car's  $C_p$ , hence  $C_p$  at  $b$  is similar for 3, 6 and 8-car group trains. However, as the train length increases, the negative pressure crest of the tail car (i.e., at the streamlined transition) decreases significantly (i.e.,  $e_1 > e_2 > e_3$ ). This indicates that as the train length increases, thicker boundary layer is noted at the rear car region (as noted in Section 4.2), while the  $C_p$  on the tail car decreases, causing a reduction in the tail car's drag, as listed in Table 4. A similar observation has been made in the work of Chen *et al.* (2022). As stated in Section 4.2, because of the internal windshield in Case 1, flow separation occurs in the windshield region. This causes a large fluctuation of  $C_p$  in those regions.

In Case 2, with the presence of external windshields in all except the first inter-carriage section, the pressure distribution at the train's symmetry centreline is not impacted much, as the variation of  $C_p$  only occurs at  $b$  on the head car,  $l_1$  at the first windshield (i.e., an internal windshield) and  $e_1$ ,  $e_2$  and  $e_3$  at the tail car. In Case 3, the internal windshield is located at the last inter-carriage gap of the trains; therefore, the  $C_p$  variation at the windshield areas only occurs at  $l_2$  for 3-car,  $l_5$  for 6-car and  $l_7$  for 8-car group trains. However, in Case 4 no fluctuations of  $C_p$  are observed as an external windshield is employed in this case. Therefore, only the head and tail cars experienced large changes in  $C_p$  as the train length increased.

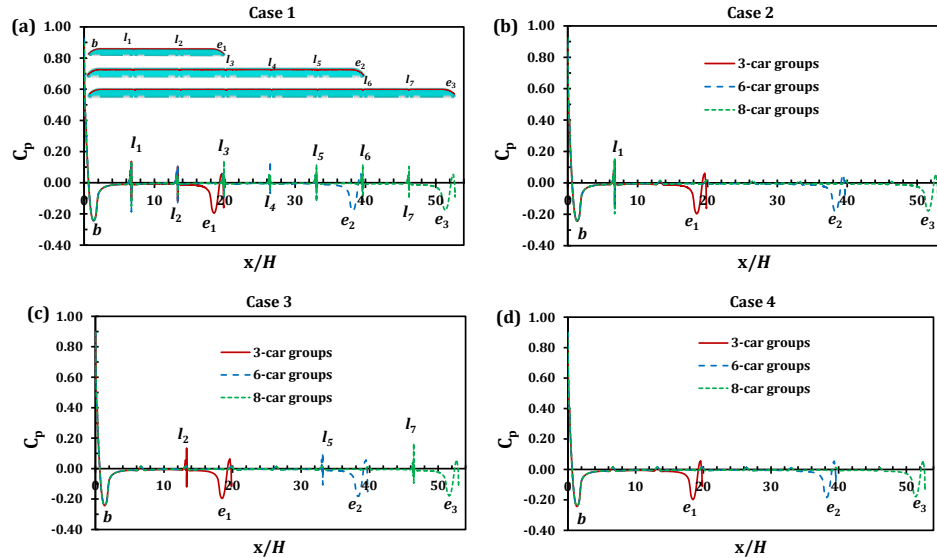


**Fig. 13.**  $C_p$  distributions at the upper symmetry centreline for 3, 6 and 8-car group trains in Cases 1–4 respectively.

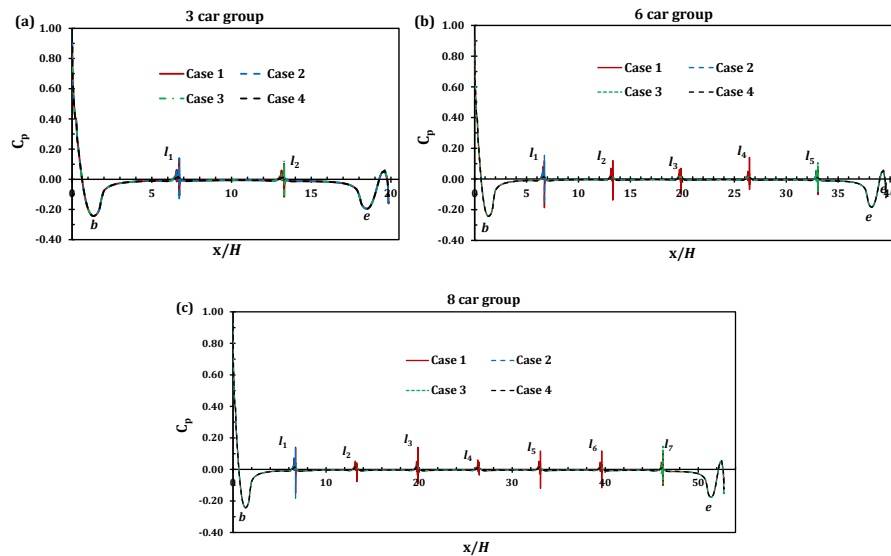


**Fig. 14.** Comparison of  $C_p$  distributions on the symmetry centreline of Cases 1–4 for the 3, 6 and 8-car group trains respectively.

Figure 14 highlights the  $C_p$  distributions on the symmetry centreline of Cases 1–4 for the 3, 6 and 8-car groupings respectively.

For the 3-car grouping, all the cases show the same  $C_p$  value at  $b$  and  $e$ ; however, a variation is observed at the windshield region. Since the windshield configurations of Case 1 and Case 2 are the same at the first windshield area, similar  $C_p$  peaks are observed at  $l_1$ . Also, similar peaks are observed for Case 1 and Case 3 at  $l_2$ ; however, for Case 4, no fluctuation is observed, as an external windshield is used in the inter-carriage region. A similar trend of  $C_p$  distribution is observed at  $b$  and  $e$  for 6 and 8-car

group trains; nevertheless, the peak value in Case 1 decreases at  $l_3$  and is followed by  $l_5$  for the 6-car group train, while this reduction is observed at  $l_2$  and  $l_4$  for the 8-car group train. This variation in the  $C_p$  peaks in different windshield regions in Case 1 causes a variation in the values of the middle car's drag, even though a decrease in drag is expected as the length increases due to a steady increase in the boundary layer thickness. For Case 2 and Case 3, only the places with internal windshields show  $C_p$  fluctuations for both 6 and 8-car group trains. However, in Case 4, no fluctuations in the windshield areas are observed, hence only the thickness of the boundary layer becomes the most

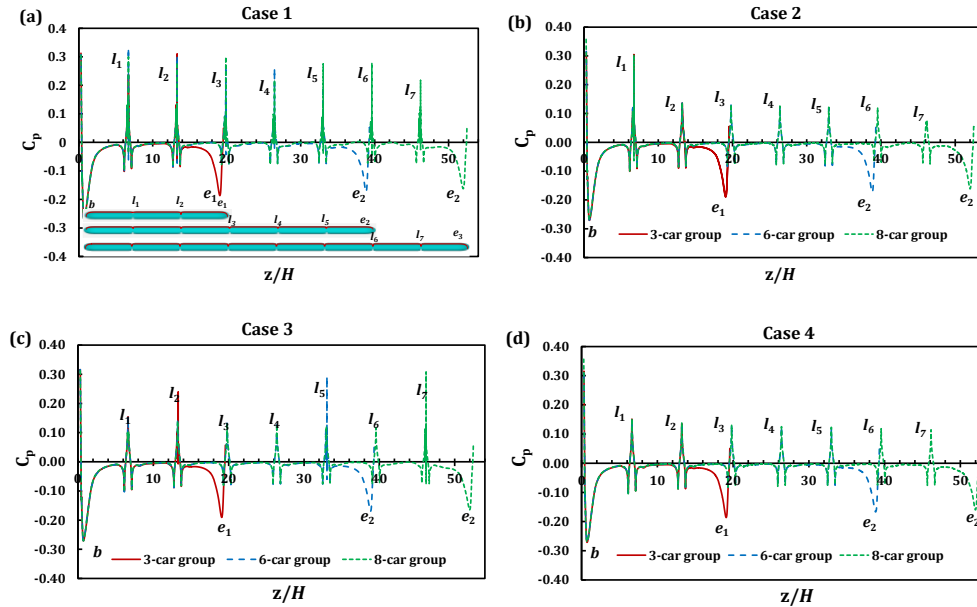


Fig. 15.  $C_p$  distributions on the train along the side-line at  $z = 0.3H$  for 3, 6 and 8-car group trains in Cases 1–4 respectively.

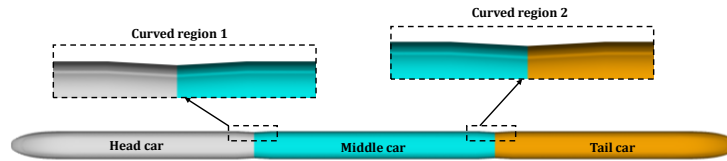


Fig. 16. The geometrical shape of the train with the non-smooth region near the windshield areas.

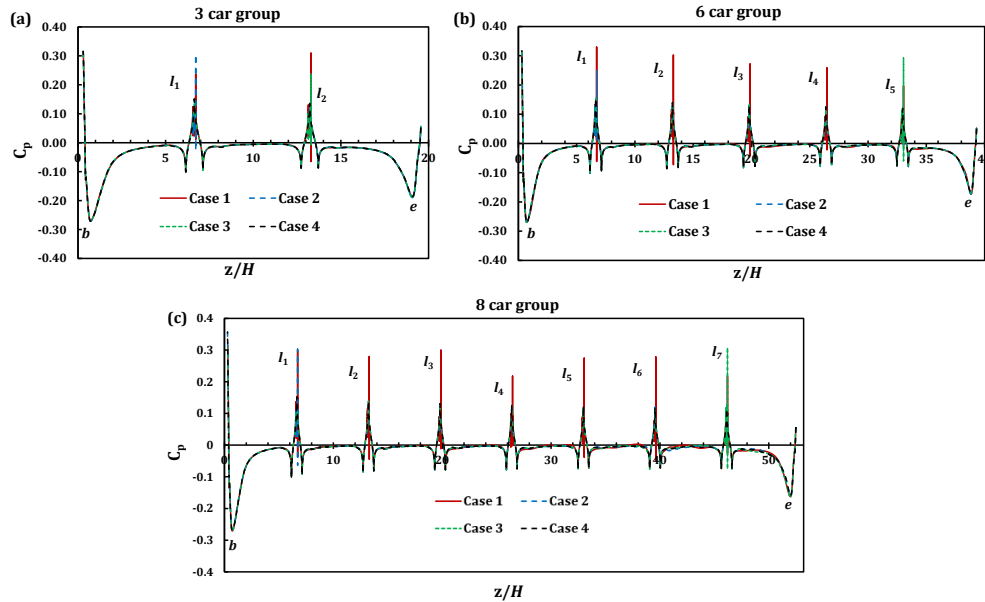
important factor that influences the train drag, contributing to a steady decrease in the middle cars' drag, as recorded in Table 4.

Figure 15 presents the  $C_p$  distributions on the train along the side-line at  $z = 0.3H$  for 3, 6 and 8-car group trains in Cases 1–4 respectively. At both the head and tail cars,  $C_p$  at  $b$  is constant and  $e_1 > e_2 > e_3$  for all cases. In Case 1, the variation of the train length causes a difference in the  $C_p$  peak at the side of the windshield regions. As the train length increases, the peak reduces. However, lower peaks are observed at  $l_4$  and  $l_7$  as compared to those at the other windshield areas. The geometry of the train is not completely smooth in the windshield areas, even with an external windshield as shown in Fig. 16. Consequently, fluctuations are observed in the windshield area along the side-line of the train, which are not visible on the symmetric centreline.

In Case 2 and Case 4, a similar decreasing trend of  $C_p$  peaks is observed in the windshield areas. The peak at  $l_1$  is much higher than those of  $l_2$ – $l_7$  for the 6 and 8-car group train in Case 2, while in Case 4, it decreases steadily from  $l_1$ – $l_7$  with an increased thickness of the boundary layer along the train. In Case 3, since the internal windshield is located at the last inter-carriage

gap section, high peak  $C_p$  values are observed at  $l_2$ ,  $l_5$  and  $l_7$  for 3, 6 and 8-car groupings. An increase in the peak value of  $C_p$  is observed in the last inter-carriage section, as the train length increases, in Case 3. This is in contrast with the observation in Case 1, which has an internal windshield at the last inter-carriage section as Case 3. Since the peak value is at  $l_7$ ,  $l_5$  and  $l_2$  in Case 3, it is expected that the tail car's drag for the 8-car grouping is greater than those of the 6 and 3-car groupings. However, the aerodynamic drag is the integral of the pressure drag (due to the surface pressure force) and viscous drag (due to boundary layer thickness). Therefore, the summation of viscous drag and pressure drag leads to a decrease in the total tail car drag with increase length of train. However, the difference between the 6 and 8-car group tail car's drag is small, as shown in Table 4.

Furthermore, Fig. 17 compares the  $C_p$  distributions along the side-line at  $z = 0.3H$  of Cases 1–4 for 3, 6 and 8-car group trains. For a 3-car group train, Case 1 and Case 2 have similar  $C_p$  peaks at  $l_1$  while in Case 3 and Case 4 it is at  $l_2$ . As the train length increases, Case 1 has higher  $C_p$  peaks at  $l_1$ – $l_4$  for a 6-car group train and  $l_1$ – $l_6$  for an 8-car group train. A higher  $C_p$  is seen in Case 3's last windshield sections as compared to Cases 1, 2, and 4.



**Fig. 17.** Comparison of  $C_p$  distributions along the side-line at  $z=0.3H$  of Cases 1–4 for the 3, 6 and 8-car group trains respectively.

## 5. CONCLUSIONS

An HST's geometry significantly affects the flow field surrounding it. This study reveals that variation of the windshield configuration and train length significantly impacts the airflow surrounding the train, which impacts the HST aerodynamic characteristics.

The head aerodynamic drag increases significantly when an external windshield is employed. When an internal windshield is employed at the first inter-carriage section, the head and tail car's drag decreases significantly. When the total drag is compared, a drag reduction of 1.5%, 1.3% and 2.0% is achieved in Case 2, Case 3 and Case 4 as compared to Case 1, for 3-car group trains. As the train length increases, the drag is decreased by 5.0%, 4.7% and 5.2% respectively, for 8-car group trains. Therefore, employing external windshields in all the inter-carriage gap sections, irrespective of the train length, demonstrates a good ability to reduce future trains' aerodynamic drag.

For the trains with internal windshields, due to the non-uniform geometry of the train surface in those regions, the flow is separated and vortices are formed at the windshield area. Asymmetric vortices emerge in the wake of Case 1, 2 and 3 at a distance close to the tail car nose, which increases with increased train length.

The boundary layer thickness increases with the train length of the train, leading to a drop in the streamwise velocity around the tail car streamlined region. Consequently, Case 1 has a thicker boundary layer profile at the upper part and the sides of the train as compared to other cases.

The reduction in the flow velocity as the train length increases results in a decrease in the negative pressure near the tail car streamline transition, thus causing a decrease in tail car drag and lift force. However, an increase in the peak value of  $C_p$  is noted in the last inter-carriage section, as the train length increases, in Case 3. This is in contrast with the observation in Case 1, which has a similar windshield configuration to that of the last inter-carriage section.

## ACKNOWLEDGEMENT

The authors acknowledge the computing resources provided by the High-speed Train Research Center and the High Performance Computing Center of Central South University, China. The research described in this paper was supported by the National Key R & D Program of China (Grant No. 2020YFF0304103-03), the Science and Technology Research Program of China State Railway Group Co., Ltd. (Grant Nos. P2019J023 and P2020J025), the Natural Science Foundation of Hunan Province, China (Grant No. 2020JJ4118), and the Initial Funding of Specially-appointed Professorship of Central South University, China (Grant No. 202045014).

## REFERENCES

- Baker, C. (2010). The flow around high speed trains. *Journal of Wind Engineering and Industrial Aerodynamics* 98(6), 277-298.
- Baker, C. (2014). A review of train aerodynamics Part 2—Applications. *The Aeronautical Journal* 118(1202), 345-382.

- CEN European Standard* (2010). Railway applications- Aerodynamics-Part 6: Requirements and test procedures for cross wind assessment.
- Chen, G., X. Li, L. Zhang, X. Liang, S. Meng and D. Zhou (2022). Numerical analysis of the effect of train length on train aerodynamic performance. *AIP Advances* 12(2), 025201.
- Dong, T., G. Minelli, J. Wang, X. Liang and S. Krajnović (2020). The effect of ground clearance on the aerodynamics of a generic high-speed train. *Journal of Fluids and Structures* 95, 102990.
- Du, J., X. F. Liang, G. B. Li, H. L. Tian and M. Z. Yang (2020). Numerical simulation of rainwater accumulation and flow characteristics over windshield of high-speed trains. *Journal of Central South University* 27(1), 198-209.
- Jia, L., D. Zhou and J. Niu (2017). Numerical calculation of boundary layers and wake characteristics of high-speed trains with different lengths. *PLOS One* 12(12), e0189798.
- Kukreja, N. and S. Jumar (2016). Aerodynamic loss in inter-car space of train and its reduction. *International Journal of Latest Trends in Engineering and Technology* 6, 80-89.
- Li, T., H. Hemida, J. Zhang, M. Rashidi and D. Flynn (2018). Comparisons of shear stress transport and detached eddy simulations of the flow around trains. *Journal of Fluids Engineering* 140(11).
- Li, T., M. Li, Z. Wang and J. Zhang (2019). Effect of the inter-car gap length on the aerodynamic characteristics of a high-speed train. *Proceedings of the Institution of Mechanical Engineers, Part F: Journal of Rail and Rapid Transit* 233(4), 448-465.
- Menter, F. R. (1994). Two-equation eddy-viscosity turbulence models for engineering applications. *AIAA Journal* 32(8), 1598-1605.
- Muld, T. W., G. Efraimsson and D. S. Henningson (2014). Wake characteristics of high-speed trains with different lengths. *Proceedings of the Institution of Mechanical Engineers, Part F: Journal of Rail and Rapid Transit* 228(4), 333-342.
- Munson, B. R., D. F. Young, T. H. Okiishi and W. W. Huebsch (2006). *Fundamentals of fluid mechanics*. John Wiley & Sons.
- Niu, J., Y. Wang, L. Zhang and Y. Yuan (2018a). Numerical analysis of aerodynamic characteristics of high-speed train with different train nose lengths. *International Journal of Heat and Mass Transfer* 127, 188-199.
- Niu, J. Q., D. Zhou and X. F. Liang (2018b). Numerical simulation of the effects of obstacle deflectors on the aerodynamic performance of stationary high-speed trains at two yaw angles. *Proceedings of the Institution of Mechanical Engineers, Part F: Journal of Rail and Rapid Transit* 232(3), 913-927.
- Niu, J., Y. Wang and D. Zhou (2019). Effect of the outer windshield schemes on aerodynamic characteristics around the car-connecting parts and train aerodynamic performance. *Mechanical Systems and Signal Processing* 130, 1-16.
- Sicot, C., F. Deliancourt, J. Boree, S. Aguinaga and J. Bouchet (2018). Representativeness of geometrical details during wind tunnel tests. Application to train aerodynamics in crosswind conditions. *Journal of Wind Engineering and Industrial Aerodynamics* 177, 186-196.
- Sun, Z. K., T. T. Wang and F. Wu (2020). Numerical investigation of influence of pantograph parameters and train length on aerodynamic drag of high-speed train. *Journal of Central South University* 27(4), 1334-1350.
- Tan, C., D. Zhou, G. Chen, J. Sheridan and S. Krajnovic (2020). Influences of marshalling length on the flow structure of a maglev train. *International Journal of Heat and Fluid Flow* 85, 108604.
- Tan, X. M. and Z. G. Yang (2022). Investigation on aerodynamic noise reduction for snow-plough of high-speed train. *Journal of Central South University* 29(5), 1735-1748.
- Tang, M. Z., X. H. Xiong, X. B. Li, J. Zhang, G. Chen and K. W. Wang (2022). Vibration characteristics of outer windshield structures of high-speed trains based on fluid-structure interactions. *Nonlinear Dynamics*.
- Tian, H. Q., S. Huang and M. Z. Yang (2015). Flow structure around high-speed train in open air. *Journal of Central South University* 22(2), 747-752.
- Tian, H. Q. (2007). *Aerodynamics of train*. China Railway Press, Beijing.
- Wang, F., Z. H. Guo, Z. L. Shi, S. Han, Y. G. Wang and J. Zhang (2022). A Study of Crosswind Characteristics on Aerodynamic Performance of High-Speed Trains on Embankment. *Iranian Journal of Science and Technology, Transactions of Mechanical Engineering*.
- Wang, J., G. Minelli, T. Dong, K. He and S. Krajnović (2020). Impact of the bogies and cavities on the aerodynamic behaviour of a high-speed train. An IDDES study. *Journal of Wind Engineering and Industrial Aerodynamics* 207, 104406.
- Xia, C., H. Wang, X. Shan, Z. Yang and Q. Li (2017). Effects of ground configurations on the slipstream and near wake of a high-speed train. *Journal of Wind Engineering and Industrial Aerodynamics* 168, 177-189.
- Xia, Y., T. Liu, H. Gu, Z. Guo and W. Li (2020). Aerodynamic effects of the gap spacing between adjacent vehicles on wind tunnel train models.

*Engineering Applications of Computational Fluid Mechanics* 14, 835-852.

- Yang, B., X. H. Xiong, Z. Li, X. B. He, P. H. Xie and M. Z. Tang (2022). Feasibility of replacing the 3-coach with a 1.5-coach grouping train model in wind tunnel experiment at different yaw angles. *Journal of Central South University* 29(6), 2062-2073.
- Zhang, J., A. Adamu, X. C. Su, Z. H. Guo and G. J. Gao (2022a). Effect of simplifying bogie regions on aerodynamic performance of high-speed train. *Journal of Central South University* 29(5), 1717-1734.
- Zhang, J., A. Adamu, S. Han, F. Wang, G. J. Gao and F. Gidado (2022b). A numerical investigation of inter-carriage gap configurations on the aerodynamic performance of a wind-tunnel train model. Proceedings of the Institution of Mechanical Engineers, Part F: *Journal of Rail and Rapid Transit*, 1-17.
- Zhang, J., J. Wang, Q. Wang, X. Xiong and G. Gao, (2018). A study of the influence of bogie cut outs' angles on the aerodynamic performance of a high-speed train. *Journal of Wind Engineering and Industrial Aerodynamics* 175, 153-168.
- Zhou, D., L. Wu, C. Tan and T. E. Hu (2021). Study on the effect of dimple position on drag reduction of high-speed maglev train. *Transportation Safety and Environment* 3(4), tdab027.